

https://dspace.org/

An UltrathinWalled Foam Heat Pipe

YX Wang; CQ YU; K Kang; Michael Atkins; T Kim

https://hdl.handle.net/10539/42054
WOS

Downloaded from a DSpace repository. https://dspace.org/

Check for updates

ASME Journal of Heat and Mass Transfer
Online journal at:
https://asmedigitalcollection.asme.org/heattransfer

Yi Xiang Wang
Department of Mechanical Engineering,
Chonnam National University,
Gwangju 61186, South Korea
e-mail: wyx9909@126.com

Cheng Qin Yu
Department of Mechanical Engineering,
Chonnam National University,
Gwangju 61186, South Korea;
Department of Mechatronics, Jiaxing Vocational
and Technical College,
Jiaxing, Zhejiang 314036, China
e-mail: yuchengqin_clara@outlook.com

Kiju Kang[1]
Department of Mechanical Engineering,
Chonnam National University,
Gwangju 61186, South Korea
e-mail: kjkang@chonnam.ac.kr

Michael D. Atkins
School of Mechanical, Industrial, and
Aeronautical Engineering,
University of the Witwatersrand,
Johannesburg 2000, South Africa
e-mail: michael.atkins@wits.ac.za

Tongbeum Kim
College of Aerospace Engineering,
Nanjing University of Aeronautics and
Astronautics,
Nanjing 210016, China
e-mail: tongbeum.kim@nuaa.edu.cn

An Ultrathin-Walled Foam Heat Pipe

We present an advanced thermal solution for capillary-driven heat pipes that addresses a fundamental problem with existing heat pipes being inefficient space utilization and limited thermal spreading performance. Our solution features the full occupation of open-cell foam core and ultrathin-walled envelope—an ultrathin-walled foam heat pipe (uFHP). A copper layer is formed sequentially via electroless—and electroplating, and envelopes a tailored block of open-cell foam core, followed by a series of chemical surface treatments that create a nanoscale texture on the foam ligament and envelope's inner surfaces for improved capillary pumping. The high porosity foam core ($\varepsilon = 0.974$) for vapor passaging and wicking, and the ultrathin-walled envelope of 50 μm, make the uFHP remarkably lightweight (64% lighter than commercial heat pipes). Further, conductive spreading and convective transfer of heat from vapor and condensate by foam ligaments to the envelope, increase overall heat rejection. Consequently, the thermal resistance and evaporator temperature are reduced. More importantly, the uFHP could be tailored into any cross-sectional (e.g., noncircular) shape. This tailorable uFHP can be an alternative heat pipe thermal solution for extreme compact operations that require improved thermal performance. [DOI: 10.1115/1.4065352]

1 Introduction

Capillary-driven heat pipes are utilized as a key element of thermal management systems for high-power electronic components, e.g., CPU/GPU chips due to their low cost, design flexibility, and good thermal spreading capability [1–3]. This device spreads heat via latent heat conversion of a working fluid as it flows through the following primary sections of the heat pipe: (i) evaporator, (ii) vapor passage, (iii) a condenser, and (iv) a wick structure, which is all enclosed in a simple bar-type pressure chamber, termed an "envelope." The working fluid of the heat pipe is a phase-changeable medium (e.g., water, nitrogen, or sodium) whose phase transitions between liquid and vapor, depending on the operating temperature range between the evaporator and the condenser. Input heat from the high-temperature source external to the device is transferred to the evaporator and then spread to the condenser via the vapor passage. An external heat rejection system (e.g., fins and cooling fan) is typically employed at the condenser end.

Among the four components of the heat pipe, the design of the wick structure greatly determines the overall thermal spreading capability. The wick is characteristically a porous medium with small pore dimensions to provide capillary pumping of the working fluid, "condensate" *from* the condenser back *to* the evaporator to complete a thermodynamic cycle. Existing wick structure designs include sintered powders [4], grooves [5], and screen meshes [6]. Wicks made of sintered copper powders are predominant, albeit with several shortcomings.

Traditional sintered powder wicks are mostly monoporous with a single characteristic pore size whereas recently developed sintered powder wicks are bi-porous with two distinguishable characteristic pore sizes [7]. A monoporous sintered powder wick may give rise to high hydraulic resistance, causing the evaporator to dry out [8]. Dry-out occurs when the condensate in the wick prematurely boils off before reaching the evaporator [9] or an insufficiently filled ratio of a working fluid in the wick [10], thus the closed thermodynamic cycle becomes incomplete.

On the other hand, a bi-porous topology is characterized by two distinctive lengths in which the larger length scale reduces liquid hydraulic resistance whereas the smaller one provides sufficient capillary force [7,8,11]. Wu et al. [12] compared a monoporous to a bi-porous sintered wick structure made from a mixture of nickel

[1]Corresponding author.

Contributed by the Heat Transfer Division of ASME for publication in the Journal of Heat and Mass Transfer. Manuscript received December 28, 2023; final manuscript received March 28, 2024; published online May 6, 2024. Assoc. Editor: Yun Wang.

 Copyright © 2024 by ASME

Downloaded from http://asmedigitalcollection.asme.org/heattransfer/article-pdf/doi/10.1115/1.4065352/7332717/ht_146_08_081602.pdf by The Nanjing University Of Aeronautics & Astronautics user on 07 May 2024

(size ~ 3 μm) and PMMA polymer particles (size: 250–297 μm) in a 35% volume proportion and demonstrated that the thermal resistance of the bi-porous wick decreased by about 60%, and the highest heat load was increased by about 130%.

In addition, highly porous metallic foams constituted by stochastic open pores are another example of bi-porous media; the co-existence of d_{pore} and d_{cell} (Fig. 1). The metallic foam pores can be as small as 40 μm, which enhance capillary forces while the high porosity corresponds to high permeability, and hence increase capillary pumping [13]. Zhou et al. [14] observed that a copper metallic foam with smaller pore wick structures provides a much larger capillary force to drive the cycle of the working fluid. Therefore, the copper foam as a wick structure achieved better thermal performance (i.e., shorter startup time and decreased thermal resistance).

Despite the limitations of monoporous sintered powder wicks these structures have widespread utilization in capillary-driven heat pipes for electronics cooling applications [2]. Due to reasonable capillary pumping, resultant heat spreading, and cost-effective fabrication. In a typical manufacturing process, a cylindrical envelope is chosen for the desired length and diameter. Afterwards, copper powders are sintered onto the inner surface of the envelope at ~ 900 °C [15]. Particularly for the midsection (e.g., vapor passage and wick), a special mandrel is inserted before filling the wick volume with sintered powders and removed after sintering. The particle size, sintering temperature, and time are precisely and iteratively controlled to achieve designated parameters for sintered powder wicks [16]. In summary, after the internal shape (typically cylindrical) and dimensions of the envelope are designed, the detailed geometrical parameters of wick, e.g., shape and thickness are subsequently determined. Therefore, particularly for bar-type capillary-driven heat pipes, the envelope design has been largely limited to being cylindrical with a circular cross section. The conventional circular, cylindrical form factor of these heat pipes often results in low utilization of available space surrounding the device since these often do not conform well to the external space. Such limitation becomes exacerbated for compact operations.

The requirement for compact thermal management devices in miniaturized electronics (e.g., smartphones and tablets) has resulted in the so-called "ultrathin heat pipe (UTHP)," which typically takes the form of flattened circular section sintered copper powder heat pipes, or thin wick sheet sandwiched between two metallic sheets. Such UTHPs have a thickness of ≤ 2.0 mm to provide high thermal dissipation performance for space-limited electronics [17]. Several UTHP designs were developed and tested, for example, Cui et al. [18] developed a striped super-hydrophilic (i.e., thermal oxidation treated) copper mesh wick structure, with a total thickness of 0.68 mm and minimum thermal resistance of 0.26 K/W, based on the temperature difference between the evaporator and the condenser ends. Other works, such as Li and Lv [19] have reported similar minimum thermal resistance values for UTHP where at condenser cooling temperatures of 25 °C, 30 °C, 35 °C, and 40 °C, the thermal resistances were 0.260 K/W (84 W), 0.221 K/W (96 W), 0.196 K/W (108 W), and 0.215 K/W (96 W), respectively. In addition, their 1.0 mm thick, sintered hybrid powder wick UTHP achieved over four times the effective thermal conductivity of a flat copper plate thermal spreader. While UTHP's provide compact cooling for miniaturized electronics the minimal thermal resistance performance appears to have reached an asymptotic limit of approximately 0.2 K/W [17].

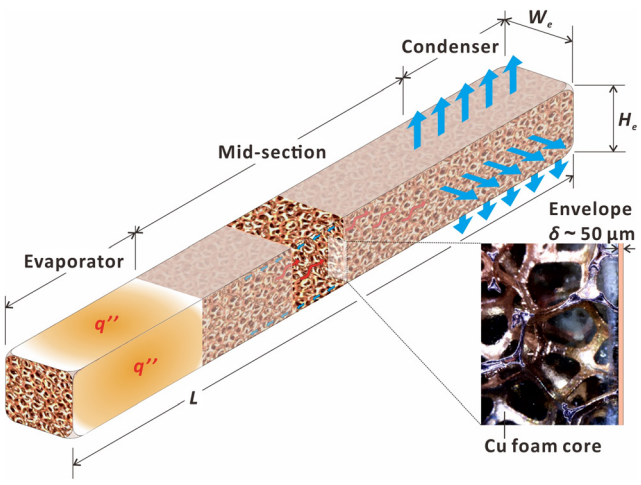


Fig. 1 A tailored ultralight foam heat pipe (uFHP) with an ultrathin-walled envelope

An alternative design strategy for capillary-driven heat pipes and vapor chambers is to utilize metal foams that partially and fully occupy the internal volume since metal foams are intrinsically bi-porous by nature, due to the two characteristic pore sizes that constitute the metal foam structure. The pioneering work by Phillips [20] integrated a metal foam structure into heat pipes for space applications. He noted that the permeability-to-effective capillary radius ratio (K/r_{eff}) is a key parameter governing the maximum heat flux at the evaporator and that foam wicks favorably obtained increased (K/r_{eff}) ratios compared to conventional sintered and screen-type wicks. For example, the (K/r_{eff}) ratio of the 200-mesh screen was roughly one order of magnitude less than that of the metal foam. Subsequent work by Carbajal et al. [21] proposed a foam vapor chamber—heat pipe sandwich panel for simultaneous thermal spreading and mechanical load-bearing applications. They found that high permeability and porosity of the metal foam facilitated vapor flow due to low-pressure drop, and its solid ligaments mechanically connected to the envelope, increased overall thermal spreading. Queheillalt et al. [22] developed a vapor chamber with a 90 PPI foam insert after longitudinal compression, that achieved a more uniform temperature distribution than a solid plate. Hansen et al. [23] characterized flow parameters (e.g., K and r_{eff}) of compressed metal foams with different levels of wick compression. They showed that the ratio K/r_{eff} of compressed foams ranged from 0.54 μm to 2.44 μm and sintered metal powders was roughly one order of magnitude lower ranging from $K/r_{eff} = 0.05$ μm to 0.77 μm. Thus, compressed foam exhibited greater permeability for a given effective capillary radius. Dhanabal et al. [24] inserted copper foam columns into a flat heat pipe's vapor passage and found that increasing the wick volume improves the FHP performance, due to the decreased thermal resistance with increased fluid movement in these additional wick columns. A series of analytical and experimental works by Shirazy and Frechette [25,26] reported that the partial replacement of the sintered powder wick having a porosity (ε) of 0.52, with the copper foam of 60 pores per inch and $\varepsilon = 0.75$ gave rise to five times larger K/r_{eff} ratio.

It should be noted that permeability (K) and effective capillary radius (r_{eff}) can be altered also by surface treatments to further increase the K/r_{eff} ratio and to improve capillary pumping. The chemical oxidation method is the most widely used fabrication process due to its controllable reaction conditions, simple operation process, and ability to treat most wick structures [27]. Nam et al. [28] fabricated Cu oxide (CuO) layers on sintered copper powder wick surfaces by mixing chemical solutions with alkali agents and oxidants. The chemical treatment increased the K/r_{eff} ratio by an order of magnitude (for water), which resulted in a 70% higher critical heat flux of a heat pipe. Similar chemical oxidation methods were carried out by Shum [29] and Yang [30] on copper foams, and showed that the superhydrophilic CuO layers significantly improved the capillary performance ($K/r_{eff} = 3.92$) of a copper foam wick.

In this study, we have advanced the capillary-driven heat pipe design by introducing two distinct solutions to address the following limitations of conventional heat pipes as: (i) a high form factor, leading to poor utilization of available space due to the typically circular, cylindrical shape and (ii) moderate pumping and heat transport performance (i.e., thermal resistance) attributed to suboptimal K/r_{eff} ratio achieved from conventional wicks. To squarely address these limitations we have first, tailored an *orthogonal* block of high porosity open-cell copper foam as the vapor passage and wick, which fully occupies a predetermined

Downloaded from http://asmedigitalcollection.asme.org/heattransfer/article-pdf/doi/10.1115/1.4065352/7332717/ht_146_08_081602.pdf by The Nanjing University Of Aeronautics & Astronautics user on 07 May 2024

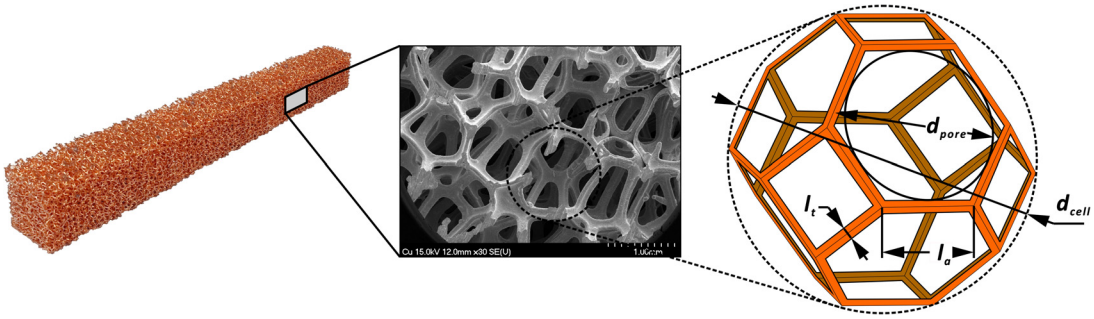


Fig. 2 Open-cell copper (Cu) foam with 60 pores per inch (PPI) with a tetrakaidekahedron unit cell [25]

shape of an envelope, with an improved form factor for compact thermal management (e.g., thin heat spreader). Afterwards, the ligaments of the tailored foam core undergo a series of super-hydrophilic chemical treatments, the so-called "blackening" to improve capillary pumping. As a result, a nanoporous texture is created on the ligament surfaces. Hence, micrometer-scale cells and pores of the foam core and nanometer scale pores of the texture on the ligaments co-exist, participating in vapor passaging and wicking as a fully functioning heat pipe. Secondly, an ultrathin layer of tens of micrometers is integrally formed to envelope the tailored foam block via electroless-and electroplating—forming an "ultrathin-walled (uFHP)" envelope. Pore-based mechanical load bearing of the foam core makes the ultrathin-walled envelope possible (Fig. 1). In sharp contrast to cylindrical sintered powder wick heat pipes and "ultrathin heat pipes" where buckling and yielding loads repeatedly exerted on the whole envelope surfaces, these loads locally apply on each outer pore of the foam core of the uFHP. The ligaments constituting these pores support the loads and thus further thinning of the envelope wall is feasible. These unique mechanical and topological aspects create flexibility for the cross section of the heat pipe to be of any shape, and not constrained to be of a cylindrical form. This article also details the fabrication of our new heat pipe design and quantifies the thermal characteristics in sharp contrast to an existing original equipment manufacturer (OEM) heat pipe that is wicked with sintered copper powders and enveloped by a cylindrical copper tube.

2 Materials and Methods

2.1 Tailored Foam Topology. The topological parameters of an open-cell copper (Cu) foam core and integration into a capillary-driven heat pipe are detailed. A block of open-cell Cu foam, 60 pores per inch (PPI) with dimensions of 90 mm (in length) by 4.4 mm (in height) by 4.4 mm (in-depth), was tailored (Fig. 2). The unit cell of the Cu foam may be represented by a tetrakaidekahedron [31], and the porosity of the unit cell was measured to be $\varepsilon = 0.975$. The length (l_a) and thickness (l_t) of foam ligaments constituting the tetrakaidekahedron unit cell were characterized based on scanning electron microscope (SEM) images. The cross-sectional shape of the present foam specimen's ligaments is roughly triangular, but for simplicity, we define the ligament thickness (l_t) as the thickness of its projection. Our statistical data show that l_a spans between 0.2 mm and 0.9 mm with a mean value of 0.412 mm $\pm$0.009, and l_t varies from 0.14 mm to 0.18 mm with a mean value of 0.159 mm $\pm$0.002 (Appendix A Fig. 8). Based on these mean values, the representative pore size (d_{pore}) is estimated from Eq. (1) [32] to be 0.7 mm while the cell size (d_{cell}) is estimated from Eq. (2) to be 1.165 mm [13]

$$d_{\text{pore}} = \sqrt{3} l_a \tag{1}$$

$$d_{\text{cell}} = 2\sqrt{2} l_a \tag{2}$$

The two scales, d_{pore} and d_{cell}, co-exist within the Cu foam core as a bi-porous medium that balances permeability and capillary pressure. It should be noted that in contrast to the topological specification provided by an original equipment manufacturer (OEM), e.g., 60 PPI (d_{pore}~0.423 mm), there is a noticeable difference, d_{pore} (measured and estimated) = 0.7 mm versus d_{pore} (OEM) = 0.423 mm.

2.2 Fabrication and Treatment. We aim to encapsulate a monolithic foam structure in an ultrathin-walled chamber that works as a capillary-driven heat pipe, to achieve a compact thermal management device with enhanced thermal performance. To this end, we have devised a fabrication process that begins with preparing a metal-polymer template as illustrated in Fig. 3(*a*). Firstly, an open-cell Cu foam block with 60 PPI was tailored by an electric discharge machine according to a predetermined shape and was dipped in a pool of a cold-mounting resin. The cold-mounting resin is a polymethyl-methacrylate (PMMA) resin that was polymerized under a pressure of 7 bar at room temperature for the suppression of bubble formation during curing. After the polymerization of the cold-mounting resin that fully infiltrated the voids of the tailored foam core, the block of foam-PMMA was machined to remove the excessive PMMA on the outer faces. The machined and polished exterior faces of the foam-PMMA block exhibits clear bonded interfaces between the foam ligaments and the void-filling PMMA.

Electroless plating and electroplating were subsequently conducted to deposit a thin copper layer that encapsulated the foam-PMMA specimen as an envelope of our final foam heat pipe. The copper layer metallurgically joined the foam ligaments' cross section that were cut flush with the exterior surfaces of the foam-PMMA specimen. The cut individual foam pores on the exterior surfaces provide mechanical support for the layer for buckling load during idling and yield load during heat piping. Its fabrication process is illustrated in Fig. 3(*b*) and detailed as follows.

Firstly, electroless plating deposited a thin Cu layer at a predetermined rate of 1.5 μm/hour for 2 h on the polished surfaces of the foam-PMMA specimen. As a result, the metallurgical joints between the deposited Cu layer of 3.0 μm and the cut foam cells flush with the exterior surfaces were established. The specific conditions for the present electroless plating are summarized in Table 2 with its reaction expressed as

$$Cu^{2+} + 2HCOH + 4OH^- \rightarrow Cu + H_2 + 2H_2O + 2HCOO^- \tag{3}$$

Here, the *p*H value of the Cu electroless plating solution was adjusted to 12.5 by adding sodium hydroxide and formaldehyde was used as the primary reducing agent.

Cu electroplating with a current density of 3.5 amperes/dm^2 subsequently deposited another Cu layer of 48 μm in 4 h at room temperature by three additives; leveler 5 ml/L, accelerator 10 ml/L, and suppresser 10 ml/L. A phosphor copper plate was used as the anode material and the direct electric current of 0.14 A was applied, which caused the copper in the anode to lose electrons and ionize into copper ions.

Ni-P electroless plating is a well-known process for excellent corrosion-resistance, which can prevent the heat pipe envelope oxidation during subsequent chemical treatments. Ni-P electroless plating deposited a 2 μm thick corrosion-resistant layer on the

Downloaded from http://asmedigitalcollection.asme.org/heattransfer/article-pdf/doi/10.1115/1.4065352/7332717/ht_146_08_081602.pdf by The Nanjing University Of Aeronautics & Astronautics user on 07 May 2024

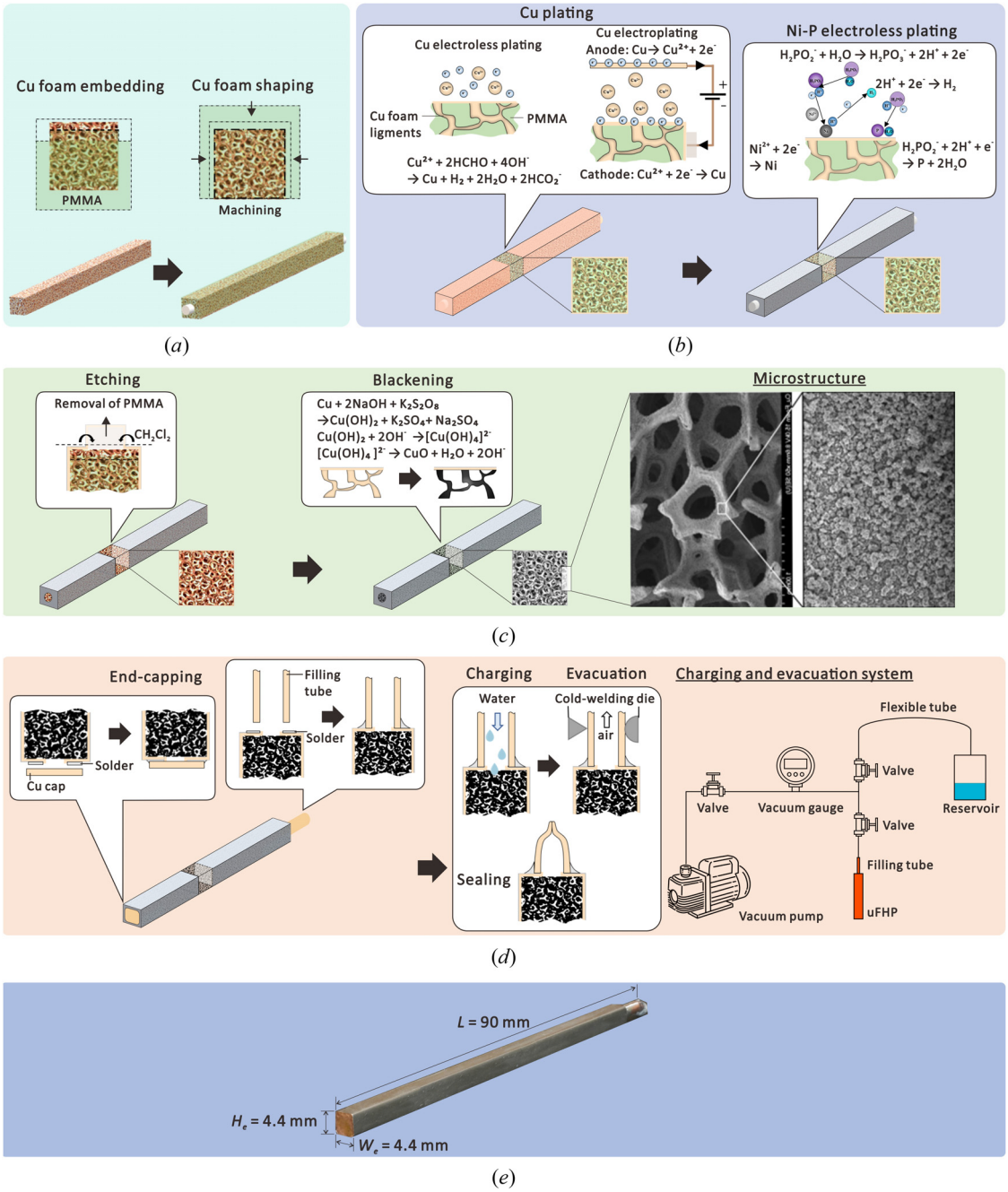


Fig. 3 Schematics of fabrication process of an ultralight foam heat pipe (uFHP): (*a*) Cu foam tailoring, (*b*) enveloping, (*c*) PMMA etching and blackening, (*d*) end-capping, DI water filling and sealing, and (*e*) a complete foam heat pipe with an ultrathin-walled envelope

exterior surfaces of the envelope. The processes and solutions for Ni-P electroless plating applied are summarized (in Table 2). The *p*H level of the Ni-P electroless plating solution was adjusted to 4.0.

To realize internal open-cell foam structures, the PMMA needed to be removed from the foam-PMMA specimen that was enveloped by a thin Cu layer. To this end, the foam-PMMA specimen was dipped in a dichloromethane-filled pool for six days at room temperature as illustrated in Fig. 3(*c*)—etching. As a result, only the foam ligament structures and thin Cu layer with the joints between the Cu layer and the outermost foam cells flush bonded with the inner surface of the Cu layer remained.

After which, the surfaces underwent a series of chemical treatments. Firstly, the specimen was dipped into an acid agent (5 wt% HCL) that removed copper oxide layers on the foam ligament surfaces and the inner surfaces of the envelope (thin Cu layer). Secondly, another treatment—the so-called "blackening" was implemented for super-hydrophilicity [27] as illustrated in Fig. 3(*c*) by a blackening solution (7.5 g/L NaOH and 1.5 g/L $K_2S_2O_8$ mixture [33]). The whole chemical treatment may be expressed as

$$Cu + 2NaOH + K_2S_2O_8 \rightarrow Cu(OH)_2 + K_2SO_4 + Na_2SO_4 \quad (4)$$

$$Cu(OH)_2 + 2OH^- \rightarrow [Cu(OH)4]^2 \quad (5)$$

$$[Cu(OH)_4]^{2-} \rightarrow CuO + H_2O + 2OH^- \quad (6)$$

The blackened surfaces exhibit a nanoporous texture as shown by a scanning electron microscopic (SEM) image in Fig. 3(*c*).

Next, the specimen is prepared for charging, evacuation, and sealing, as shown in Fig. 3(*d*). To make the specimen able to be a

Downloaded from http://asmedigitalcollection.asme.org/heattransfer/article-pdf/doi/10.1115/1.4065352/7332717/ht_146_08_081602.pdf by The Nanjing University Of Aeronautics & Astronautics user on 07 May 2024

Table 1 Parametric comparison of both OEM and uFHP specimens

	OEM heat pipe	Ultrathin-walled foam heat pipe (uFHP)
		
External dimensions	$L = 90$ mm, $D_e = 5.0$ mm	$L = 90$ mm, $W_e = 4.4$ mm, $H_e = 4.4$ mm (for capillary rise tests, $W_e = 8.0$, $H_e = 8.0$ mm)
Envelope	Copper tube Wall thickness, δ: ~400 μm Weight: ~4.7 g	Ni-P coated copper layer Wall thickness, δ: ~50 μm Weight: ~0.8 g
Wick/insert	Sintered powders Weight: ~0.9 g Particle size: 100–150 μm and 150–250 μm	Blackened 60 PPI copper foam Pore size, d_{pore}: ~423 μm Porosity, ε: ~0.974 Weight: ~0.3 g
Working fluid	DI water Weight: ~0.4 g Filling ratio (FR): ~32%	DI water Weight: ~0.52 g Filling ratio (FR): ~30%
Total weight (m)	~6.0 g	~2.2 g (inclusive of the soldering agent and filling tube)
External volume (V_e)	~1.77 cm^3 ($= \pi D_e^2/4 \times L$)	~1.74 cm^3 ($= W_e \times H_e \times L$)
Effective density ($\rho_{eff} = m/V_e$)	~3.39 g/cm^3	~1.26 g/cm^3

Table 2 Processes and solutions for Cu electroless plating and Ni-P electroless plating

Process	Process	Time (minute)	Temperature (°C)	Solution
Cu electroless plating	Cleaning	2	25	IPA
	Cleaning	2	25	DI water
	Predipping	3	25	5% HCl
	Sensitization	4	40	$SnCl_2{\cdot}2H_2O$ (10 g/L) 35% HCl (20 ml/L)
	Activation	2	25	$PdCl_2$ (1 g/L)
	Cu electroless plating	120	40	ELC-250 (A) (70 ml/L) ELC-250 (B) (40 ml/L) $NaH_2PO_2{\cdot}H_2O$ (40 g/L) HCHO (20 ml/L)
Ni-P electroless plating	Cleaning	2	25	DI water
	Predipping	3	25	5% HCl
	Sensitization	2	25	$SnCl_2{\cdot}2H_2O$ (10 g/L) 35% HCl (20 ml/L)
	Activation	2	25	$PdCl_2$ (1 g/L)
	Ni-P electroless plating	120	80	9026 AM EN (140 ml/L) 9026 BM EN (40 ml/L) 9026 DM EN (3 ml/L)

fully functioning heat pipe, one end of a specimen is soldered with a copper cap while the other is soldered with a filling tube of copper—end-capping."

A custom-built evacuation and charging system was constructed to fabricate the uFHP (Fig. 3(*d*)). The envelope housing the Cu foam insert was connected to the system via a filling tube, with a flexible film for a temporary air-tight connection. A two-stage oil-sealed rotary vane vacuum pump was used for evacuation. A digital vacuum gauge monitored the pressure inside the envelope during evacuation. A reservoir of DI water as the working fluid due to the good compatibility with the Cu foam and Cu envelope at the target working temperature ranging from 30 °C to 200 °C [34], was connected to the system with another flexible tube. In addition, to control the amount of working fluid injected into the heat pipe, three bellow-sealed valves were used to switch the mode between evacuation and charging.

The reservoir was heated and subsequently frozen by liquid nitrogen to prevent or minimize noncondensable gas (NCG) from being dissolved back in the DI water [35]. This process was repeated at least twice to minimize the NCG in the heat pipe. Subsequently, the precleaned heat pipe envelope was connected to the reservoir and evacuated at an absolute pressure of 2.1 Pa. The heat pipe specimen was charged with the working fluid via the reservoir due to the pressure difference and gravity [35]. The filling tube was sealed using a cold-welding die during evacuation.

Finally, the ultralight foam heat pipe (uFHP) is completed, consisting of a filling tube, an ultrathin-walled Cu envelope with a square cross section, and foam core. The overall length of the fabricated uFHP is $L = 90$ mm excluding the filling tube. Dimensions of the square inner chamber are $H_e = 4.4$ mm $\times$ $W_e = 4.4$ mm, and wall thickness is approximately $\delta = 50$ μm as presented in Figs. 1 and 3(*e*).

2.3 Thermal and Capillary Rise Test Setups. Thermal characterization of the uFHP was carried out using a purposely-built test rig illustrated in Fig. 4(*a*). The test rig consists of a heat pipe specimen (Fig. 1 and Table 1), five uniformly distributed cartridge heaters that simulated the external heat source (Q_{in}) at an evaporator end, a liquid-cooling unit for a condenser end, an AC power supply, an infrared (IR) camera, K-type film thermocouples, and a data acquisition unit. The heat pipe specimen was positioned vertically by a copper heating base block, with a heating area of 30 mm $\times$ 30 mm and an input power regulated from 5.0 W to 40.0 W by an AC power supply. In this particular setup, the vapor generated in the evaporator convects upwards through foam pores and the condensate moves downwards along the capillary passage configured by the inner envelope surfaces and foam pores.

Thermal grease was used between the heat pipe and heating base block to minimize contact thermal resistance. The multiple layers of

Downloaded from http://asmedigitalcollection.asme.org/heattransfer/article-pdf/doi/10.1115/1.4065352/7332717/ht_146_08_081602.pdf by The Nanjing University Of Aeronautics & Astronautics user on 07 May 2024

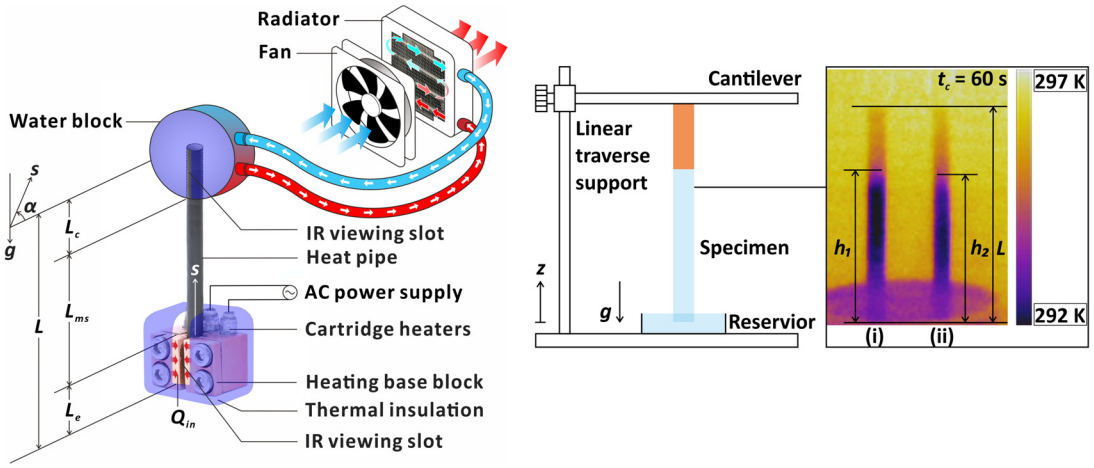


Fig. 4 Test setups: (*a*) thermal test setup with condenser section cooled by a commercial water-cooling system with Q_{in} varying from 5.0 W to 40.0 W by five cartridge heaters and (*b*) capillary rise (*h*) test setup for both (i) OEM sintered Cu powder wick and (ii) Blackened Cu foam wick, captured by a precalibrated infrared (IR) camera where $L = 90$ mm

thermal insulation tape covered the heating base block except the IR viewing slot to reduce heat loss. A commercial liquid-cooling unit was used to provide thermal rejection at the condenser section to the environment in atmospheric conditions. To mount the cooling unit on the uFHP with a square cross section, a copper heating base block was machined. The whole setup was supported by a rotation system that allows the heat piping axis (the *s*-axis) to be changed with respect to the gravitational *g*-axis whose angle is denoted by α in degree (deg) in Fig. 4a. Here, $\alpha = 0$ deg indicates that the test specimen is positioned horizontally, functioning as a heat pipe whereas at $\alpha = 90$ deg the heat pipe orientation is coincident with the gravitational axis, and the thermal spreading takes place vertically from the bottom evaporator to the top condenser, thus functioning as a thermosyphon.

To evaluate thermal spreading by the uFHP, the temperature distribution along the heat pipe span (i.e., the *s*-axis) was measured using an IR camera. Prior to measurement, the IR camera was calibrated against data obtained from film thermocouples attached to the heat pipe surface at selected locations. Temperature values from both IR camera and film thermocouples were correlated linearly as $T = 0.99T_{IR} - 0.54$ (° C) for a wide range of heat inputs to the cartridge heaters that were attached to the heat pipe. While the uFHP specimen has a square cross section, only temperatures from one surface were measured and extracted for thermal characterization. Therefore, it was necessary to justify that the temperatures on this surface are representative of those on the heat pipe. To this end, data at given span-wise locations was averaged and compared with that from the measured surface. Results indicate that the temperatures from the surface deviate only $\delta = \pm 2.1\%$ from the average temperatures along the entire span of the heat pipe.

Following a method detailed by Tang et al. [36], we purposely constructed a test setup as illustrated in Fig. 4(*b*), which includes a cantilever that holds both the wick specimen and a reservoir containing DI water. The cantilever is vertically traversable along the *z*-axis, coinciding with the gravitational (*g*-) axis. The blackened Cu foam specimen was prepared with dimensions of 8.0 mm (*H*) × 8.0 mm (*W*) × 90.0 mm (*L*). An OEM cylindrical heat pipe was cut in half by an electrical discharge machine to prepare the sintered Cu powder wick specimen. It should be noted that the Cu foam specimen is bare (i.e., without a Cu envelope attached) whereas the OEM cylindrical heat pipe is a combination of sintered powder wick and envelope. The height of the cantilever was set for both wicks to be submerged in the DI water while the precalibrated infrared (IR) camera recorded temperature variation along the span of each wick specimen at the rate of 0.2 Hz (i.e., 1 frame per 5 s), as shown by the inset of Fig. 4(*b*). The absorbed DI water acts to alter the infrared emissivity difference between the wick structure and working liquid, yielding temperature drops [36]. Thus, the capillary rise (*h*) may be estimated as a function of time.

2.4 Data Reduction Parameters and Uncertainties. Thermal resistance (R_θ) in K/W is widely used to characterize and compare the performance of heat pipes. It is a measure of thermal spreading along a given heat pipe and is defined as

$$R_\theta = \frac{T_e - T_c}{Q_{in}} \tag{7}$$

where T_e and T_c are the average temperatures of the evaporator and condenser, respectively, and Q_{in} is the total heat emitted by a heat source (or input heat). With a heater simulating the heat source, Q_{in} is typically calculated as

$$Q_{in} = \frac{V^2}{R} \tag{8}$$

where V and R are separately the voltage supplied to the heaters and electrical parallel resistance. Lower thermal resistance indicates more uniform thermal distribution along the heat pipe's span, and thus preferable.

Measurement uncertainties were estimated using a method detailed by Coleman and Steele [37], as follows. If $y = f(x_1, x_2, \ldots, x_n)$, then the uncertainty propagated by x_i in the variable y is given by

$$\Delta y = \sqrt{\left(\frac{\partial y}{\partial x_1}\Delta x_1\right)^2 + \left(\frac{\partial y}{\partial x_2}\Delta x_2\right)^2 + \cdots + \left(\frac{\partial y}{\partial x_n}\Delta x_n\right)^2} \tag{9}$$

where Δx_i is the absolute uncertainty in x_i. Equation (9) was used to estimate the uncertainty of thermal resistance (R_θ) that was associated with wall temperatures at both the evaporator and condenser ends (i.e., T_e and T_c) whose accuracy and resolution are ±2.0% and 0.06 °C, respectively. Similarly, the uncertainty of input power supplied by the AC power supply (Q_{in}) was estimated, leading to an accuracy of ±0.0015%. Thus, the uncertainty of thermal resistance was calculated to be within ±8.6%, governed predominantly by the surface temperatures.

3 Results and Discussion

3.1 Capillary Rise and Pumping. Capillary rise is a measure of capillary pumping for a given wick structure. Thus, higher

Downloaded from http://asmedigitalcollection.asme.org/heattransfer/article-pdf/doi/10.1115/1.4065352/7332717/ht_146_08_081602.pdf by The Nanjing University Of Aeronautics & Astronautics user on 07 May 2024

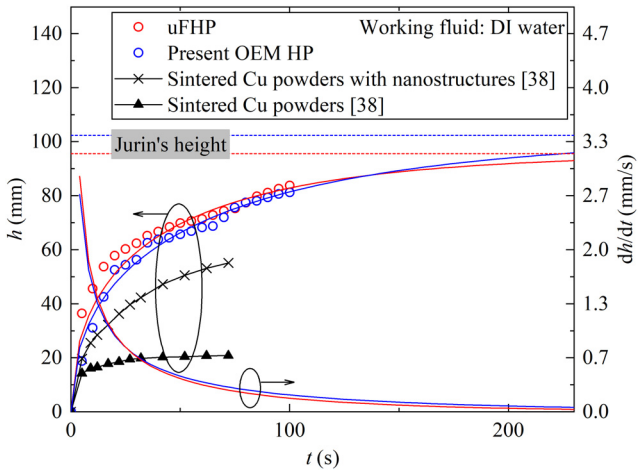


Fig. 5 Comparison of capillary rise between OEM sintered Cu powder wick measured by the present setup and alternative developmental sintered Cu powder wicks [38]

capillary rise is typically desirable for any advanced wick material/structure. For characterization, we measured the capillary rise (h) of both the blackened Cu foam wick and the OEM sintered Cu powder wick (as reference) where the details of each heat pipe are listed in Table 1. It is worth noting that the size of the blackened Cu foam specimens used is different; $W_e = 4.4$ mm and $H_e = 4.4$ mm with its length of 90 mm for the heat pipe insert whereas $W_e = 8.0$ mm and $H_e = 8.0$ mm with its length of 90 mm for the capillary rise test (see Table 1). As shown by Tang et al. [36] capillary pressure and permeability are known to be a function of porosity (ε). The size of the wicks is not expected to influence the capillary pumping, since the porosity (ε) is the same for both cases.

The capillary rise ($h(t)$) for the two test specimens in Fig. 5 behaves similarly. Based on the measured capillary rise in time (t) recorded, its rate (i.e., dh/dt) was calculated as included. There is an initial steep rise and thereafter an asymptotic decrease of the rate of capillary rise follows. This similar behavior is attributed to the capillary pressure ($\Delta P_c = 2\sigma\cos\theta/r$) during the capillary rise that is associated with pressure drop and friction forces, governed as

$$\frac{dh(t)}{dt} = \frac{\Delta P_c K}{\mu\varepsilon}\left(\frac{1}{h(t)}\right) - \frac{Kg\rho}{\mu\varepsilon} \tag{10}$$

where σ, μ, and ρ are the surface tension, viscosity, and density of DI water, separately, g is the gravitational acceleration, and K, ε, $\cos(\theta)$, and r are the permeability, porosity, contact angle, and effective radius of a given porous wick, respectively [38].

In Eq. (10), thermophysical parameters such as ρ and μ are fixed for a given working fluid. A topology-dependent parameter is K/ε for both wick structures. Given that the prior estimation of the porosity (ε) for the uFHP wick being $\varepsilon_{\text{uFHP}} = 0.974$ (Table 2) [39–47], the capillary pressure (ΔP_c) and permeability (K_{uFHP}) may be separately estimated by fitting the experimental data with the exact solution [48] for Eq. (10)

$$h(t) = \frac{\alpha}{\beta}\left[1 + W\left(-e^{-1-\frac{\beta^2 t}{\alpha}}\right)\right] \tag{11}$$

where $\alpha = \frac{\Delta P_c K}{\mu\varepsilon} = \frac{2\sigma K\cos(\theta)}{\mu\varepsilon r}$, $\beta = \frac{Kg\rho}{\varepsilon\mu}$, and $W(z)$ is Lambert W function, $z = W(z)e^{W(z)}$. Here, z is a dummy variable. Results are also included in Fig. 5 and summarized in Table 3. In comparison to the tested OEM sintered powder wick structure, the uFHP wick provides 7% lower capillary pressure and yet 3 times higher permeability with 2 times higher porosity. Collectively, the foam wick's capillary parameters function to reach roughly 10% lower Jurin's height (~100 mm), as a limit of capillary rise of a given medium.

On the other hand, the sintered Cu powders with and without nanostructures produced by chemical treatments (Li et al. [38]), achieve a capillary rise of 55.0 mm and 20.5 mm, respectively, at around $t_c = 70$ s. Here, the enhanced capillarity of the former was argued to be attributed to better hydrophilicity from smaller contact angles, because the surfaces contain the created nanoporous texture. The difference in performance between the present OEM specimen and those from Li et al. [38] may be caused by different geometrical parameters of the tested sintered Cu powders and test conditions. Despite the much higher porosity and bigger pore/cell sizes, the present Cu foam insert after the blackening provides a similar capillary pumping to the OEM sintered Cu powder wick.

3.2 Heat Piping Performance. The variation of surface temperature along individual heat pipes is indicative of thermal spreading capability. An effective heat pipe provides (a) low thermal resistance (R_θ) for minimal temperature drop between the evaporator and the condenser, and (b) lowered temperature of the evaporator (T_e) for a given heat input (Q_{in}). Thus, the characteristics of a uniform-like temperature distribution along the span (s—axis) and a low evaporator temperature in operation, are desirable.

Figure 6(*a*) shows how heat is spread from the evaporator (E) to the condenser (C) for selected input heat values, e.g., $Q_{\text{in}} = 5$ W, 15 W, 25 W, and 35 W at $\alpha = 90$ deg (functioning as thermosyphons). Data from both OEM heat pipe (wicked by sintered Cu powders) and ultralight foam heat pipe (uFHP) were compared. With the same length as the uFHP ($L = 90$ mm), the cylindrical OEM heat pipe has an outer diameter of 5.0 mm, an inner diameter of 4.2 mm (i.e., a wick thickness of 0.4 mm), and a water content of 0.4 g as summarized in Table 1. A one-to-one comparison is made of the surface temperature with respect to ambient temperature (T–T_∞), varying along the span of both heat pipes (s/L). Here, $s/L = 0.0$ and 1.0, respectively, denote the evaporator (bottom end) and condenser (top end) as both specimens were positioned vertically (i.e., $\alpha = 90$ deg) while being heated from the bottom; the condensate at the top end is fed by gravity to the bottom end.

The surface temperature for the OEM heat pipe is roughly constant within each discrete section (i.e., E, M-S, and C) but decreases in the intermediate sections between E and M-S, and M-S and C. However, for the present uFHP the surface temperature varies along the midspan, which indicates possible heat loss as the condensate moves from the condenser to the evaporator via the wick. The surface temperature of the uFHP is always lower than that of the OEM heat pipe under identical operation conditions, e.g., heat rejection at the condenser and heat input at the evaporator. This difference becomes substantial as the heat input increases, e.g., $T_e(\text{OEM}) - T_e(\text{uFHP}) \sim 30$ K at $Q_{\text{in}} = 25$ W and T_e(OEM)–T_e(uFHP) ~ 20 K at 35 W where T_e is the average evaporator temperature. A lower evaporator temperature is desirable since the attached electronic device can operate at a low temperature.

Now, both specimens are positioned horizontally (i.e., $\alpha = 0$ deg), functioning as heat pipes (Fig. 6(*b*)). In this orientation, the condensate at the C-section ($0.8 \le s/L \le 1.0$) is fed by the capillarity of the wick to the E-section ($0.0 \le s/L \le 0.2$). The surface temperature of the uFHP is also always lower than that of the

Table 3 Estimated capillary parameters by Eqs. ((7), (8)) for both uFHP and OEM heat pipe

Specimen	P_c (Pa)	K (m^2)	ρ (kg/m^3)	μ (Pa·s)	ε
uFHP	934.32	1.08×10^{-10}	998.2 (of DI water)	0.001 (of DI water)	0.974
OEM	1001.30	3.89×10^{-11}			0.470

K for open cell metal foams [39–47]: $1.0 \times 10^{-10} \sim 5.4 \times 10^{-7}$ m^2.

Downloaded from http://asmedigitalcollection.asme.org/heattransfer/article-pdf/doi/10.1115/1.4065352/7332717/ht_146_08_081602.pdf by The Nanjing University Of Aeronautics & Astronautics user on 07 May 2024

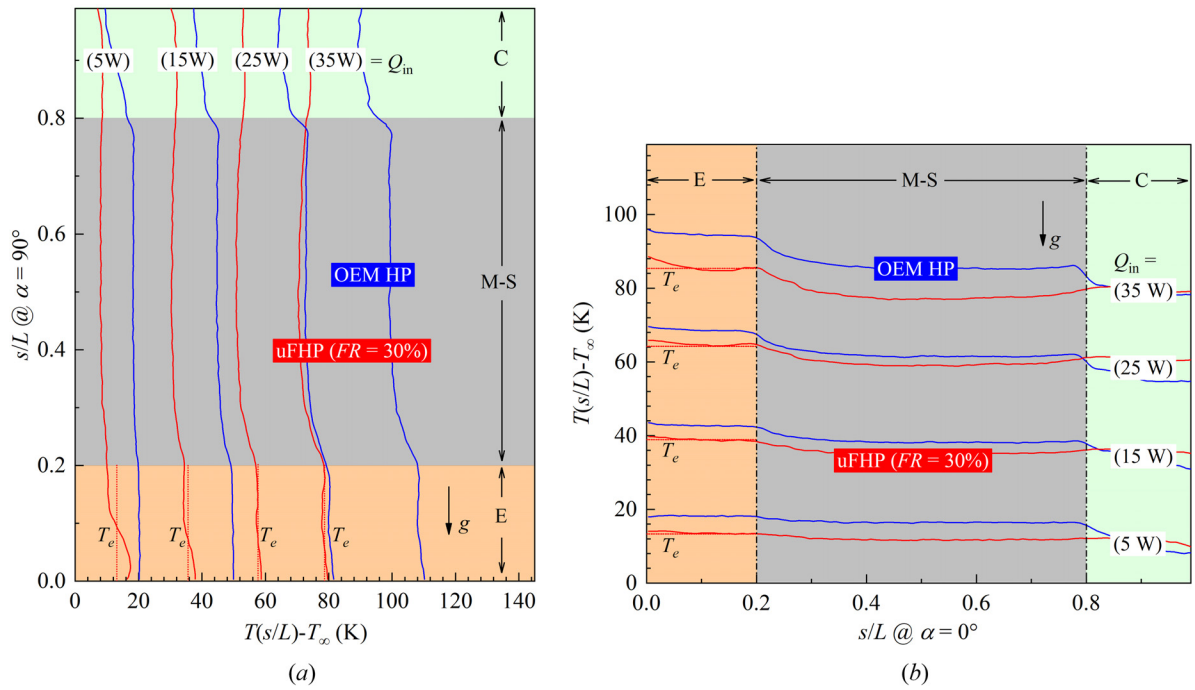


Fig. 6 Variations of surface temperature ($T(s/L) - T_\infty$) along the OEM heat pipe and uFHP for selected heat input values: (*a*) at $\alpha = 90$ deg (as thermosyphons) and (*b*) At $\alpha = 0$ deg (as heat pipes)

OEM heat pipe and the difference becomes substantially larger with increasing Q_{in}, e.g., T_e(OEM)–T_e(uFHP) ~ 10 K at $Q_{in} = 35$ W. However, the thermosyphon orientation (i.e., $\alpha = 90$ deg) achieved lower operating evaporator temperatures than the horizontal (i.e., $\alpha = 0$ deg) heat pipe configuration, likely due to the increased condensate pumping from the gravitational field.

The thermal spreading of the uFHP is further characterized by the thermal resistance (R_θ) for a given heat input, with lower values indicating favorable spreading performance. Figure 7(*a*) compares the thermal resistance of the uFHP with the OEM together with four other data sets from references [9,49–52] who tested cylindrical heat pipes with sintered Cu powders, having similar dimensions to the presently tested OEM heat pipe. All the heat pipes were at $\alpha = 0$ deg. The OEM heat pipes show the thermal resistance of 0.2 K/W $< R_\theta <$ 0.5 K/W in the heat input range up to 40.0 W while the presently tested OEM heat pipe provides $R_\theta \sim 0.5$ K/W at $Q_{in} > 25$ W. Although there exists a slight deviation from the reported values, the credibility of the present experimental setup is nonetheless established.

The thermal resistance of the uFHP decreases slightly from 0.37 K/W to 0.16 K/W as the heat input is increased from 5.0 W to 20.0 W. The further increase in the heat input up to $Q_{in} = 40.0$ W causes no visible change in thermal resistance, $R_\theta \sim 0.16$ K/W. Thus, the thermal spreading by the uFHP *exceeds* the present OEM specimen by 70% (lower thermal resistance) in the heat inputs (25.0 W $\le Q_{in} \le$ 40.0 W).

It is ideal that heat pipes perform identically, regardless of their orientation with respect to the axis of gravitation, where Dhanabal et al. [24], have identified that metal foam wicked heat pipes are able to manage more heat in any orientation. We thus characterize the variation of thermal spreading of the present OEM heat pipe and uFHP without the gravity feed. Figure 7(*b*) shows four data sets in two selected orientations, $\alpha = 0$ deg (without the gravity feed) and $\alpha = 90$ deg (with the gravity feed) for each specimen. It is apparent that after $Q_{in} = 15$ W, the gravity feed ($\alpha = 90$ deg) plays no part in spreading heat better, providing similar thermal spreading for both OEM heat pipe and uFHP. Before $Q_{in} = 15$ W, for the OEM heat pipe, both orientations give rise to the same thermal spreading whereas for the uFHP, the gravity feed results in slightly inferior thermal spreading to the case without the gravity feed ($\alpha = 0$ deg).

As a result of thermal spreading along a given heat pipe and heat rejection at the condenser, the evaporator temperature (T_e) of a heat source (e.g., electronic chip) is reduced. Therefore, this temperature may be another measure of the thermal characteristics of a liquid cooling unit that consists of a heat spreader, a liquid circulation pump, and air-side fins. Under identical cooling and operating conditions, the evaporator temperature of both heat pipes – (T_e–T_∞) is compared in Fig. 7(*c*) at 5.0 W $\le Q_{in} \le$ 40.0 W where T_∞ is the ambient air temperature. For both specimens, (T_e–T_∞) increases monotonically as the input heat increases. The decrease in (T_e–T_∞) is observed for the uFHP oriented horizontally whereas the improvement is seen for the OEM when functioning in a horizontal orientation. For both heat pipes at $\alpha = 0$ deg, the evaporator temperature of the uFHP is approximately 15% lower than the OEM heat pipe at $Q_{in} = 40$ W. For a given external volume (V_e) (i.e., OEM HP ~ 1.77 cm^3 and uFHP ~ 1.74 cm^3), the experimental testing demonstrated that the uFHP achieves higher thermal spreading for a given input heating power compared to the OEM HP, thus the power density W/cm^3 when dryout is likely to occur is enhanced using the uFHP.

The thermal transport performance of any heat pipe is dependent on the filling ratio (FR), which is the ratio of the volume of DI water (as a working fluid) used in the vessel of the heat pipe to the empty volume. In this study, both heat pipes tested (Figs. 6 and 7) have a similar filling ratio of FR = 30%. However, the uFHP filling ratio was determined based on the prior measurement (Appendix B Fig. 9). During the charging process (Fig. 3(*d*)), we varied the FR discretely for 20%, 30%, 40%, and 50%. The uFHPs with too little (FR = 20%) and too much (FR = 40% and 50%) DI water stops working as heat pipes. With FR = 20% at $Q_{in} = 5.0$ W, the uFHP works as a heat pipe reasonably well ($R_\theta = 1.0$ K/W) when the evaporator temperature is $T_e - T_\infty = 20.0$ K. However, a slight increase in Q_{in} to 10 W leads to a remarkable increase in R_θ to 4.8 K/W and in $T_e - T_\infty$ to 50.0 K. A further increase in Q_{in} causes the uFHP to stop working. With FR = 40%, a monotonic decrease in R_θ from 1.2 K/W is inter-rupted at $Q_{in} = 15.0$ W, and R_θ increases further with Q_{in}. Similarly, the evaporator temperature increases steeply after $Q_{in} = 15.0$ W. With FR = 50%, similar to the case with FR = 20%, the uFHP does not function as a heat pipe after $Q_{in} = 10$ W. The uFHP with FR = 30% works extremely well, showing superb thermal spreading and low evaporator temperature as compared and discussed in Figs. 6 and 7.

Downloaded from http://asmedigitalcollection.asme.org/heattransfer/article-pdf/doi/10.1115/1.4065352/7332717/ht_146_08_081602.pdf by The Nanjing University Of Aeronautics & Astronautics user on 07 May 2024

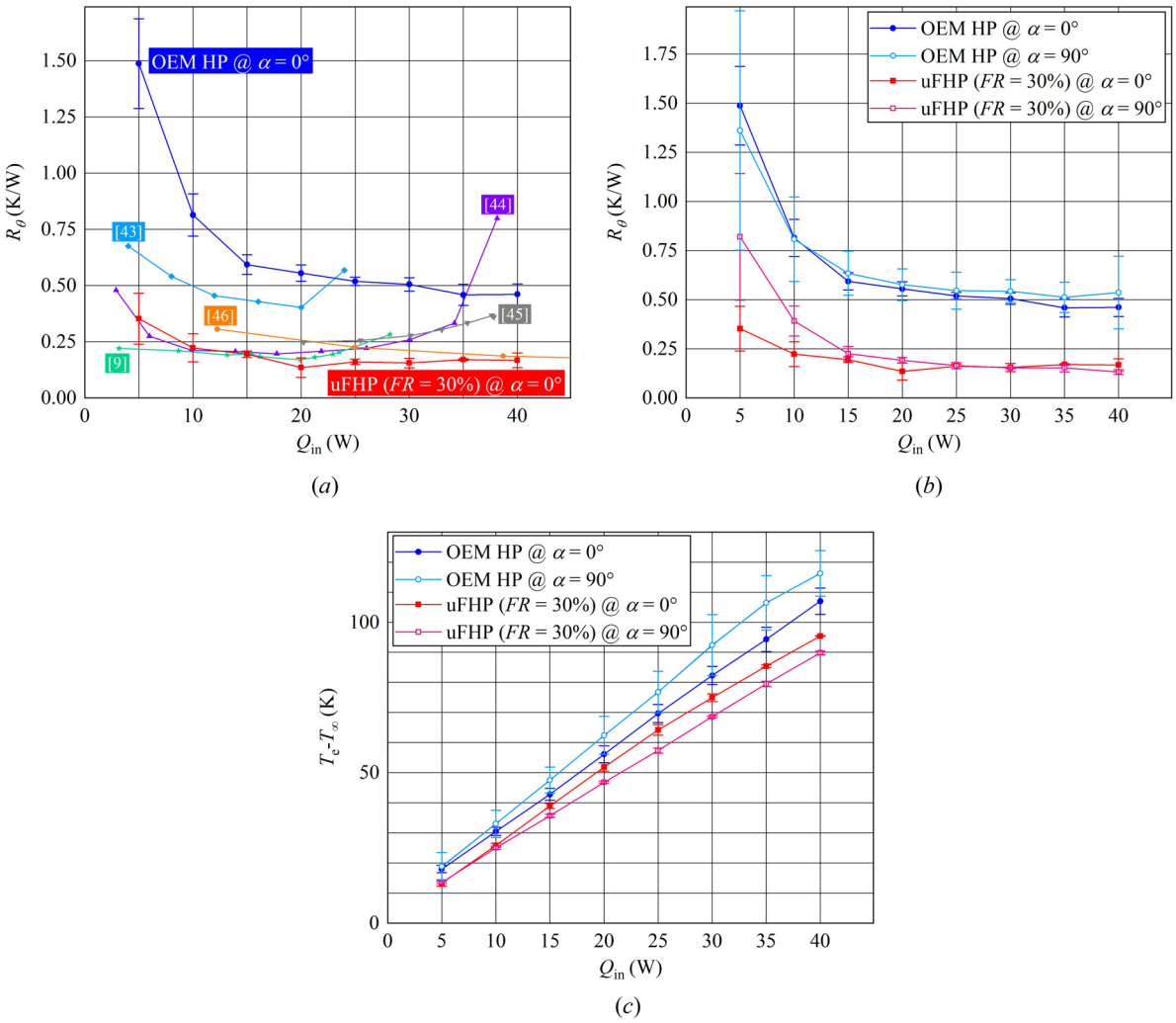


Fig. 7 Thermal resistance (R_θ) and evaporator temperature ($T_e - T_\infty$): (*a*) comparison with existing OEM heat pipes [9,49–52] for selected heat input values at $\alpha = 0$ deg, (*b*) comparison with the presently tested OEM heat pipe for both at $\alpha = 0$ deg and 90 deg, and (*c*) comparison between the presently tested OEM heat pipe and uFHP with varying heat input values for both at $\alpha = 0$ deg and 90 deg

3.3 Heat Rejection Through an Ultrathin-Walled Envelope. The uFHP with similar dimensions compared to the OEM heat pipe demonstrated improved thermal characteristics, which are summarized as follows: 70% lower thermal resistance (R_θ) and 15% lower evaporator temperature ($T_e - T_\infty$) of the uFHP than those of the OEM heat pipe, e.g., ($T_e - T_\infty$) ~ 110 °C for the OEM heat pipe versus ($T_e - T_\infty$) ~ 95 °C for the uFHP at $Q_{in} = 40$ W. Further analysis of the thermal and fluid mechanics that underpin the improved performance of the uFHP is reasoned as follows. Heat (Q_{in}) entering the evaporator vaporizes the charged DI water and is transported to the condenser via the vapor passage. During the vapor flow, some heat is lost to the surroundings through the M-S surface. In typical analysis, this surface is assumed to be adiabatic, i.e., negligible heat loss in the M-S. However, the applicability to the uFHP is questionable or uncertain. Thus, a question naturally arises as to whether the heat loss (Q_{loss}) through the M-S and reduced thermal resistance along the span of a heat pipe (R_θ) in Fig. 7(*b*) alter the evaporator temperature (T_e or $T_e - T_\infty$) as observed in Fig. 7(*c*). To this end, a thermal analysis based on an energy balance was performed.

For a capillary-driven heat pipe with heating power (Q_{in}) input imposed on the evaporator running at an average temperature (T_e). In the midsection, there is heat loss (Q_{loss}) through the envelope wall to the surroundings at ambient conditions: heat transfer occurs through the heat pipe wall to the surroundings. The condenser has an average temperature (T_c) where heat is removed (Q_{out}) via convective cooling. The conservation of energy (Appendix C) gives the evaporator temperature expressed as

$$T_e = \frac{Q_{in}}{UA} + R_\theta Q_{in} + T_\infty - \frac{Q_{loss}}{UA} \tag{12}$$

Here, T_∞ is the ambient temperature, U is the overall heat transfer coefficient and A is the heat transfer area. The final expression, Eq. (12) explicitly indicates that for given heat input through the evaporator end (Q_{in}) and heat rejection at the condenser end by convection (UA ($T_c - T_\infty$)) of a heat pipe, both thermal resistance along the heat pipe span (R_θ) and heat loss through the midsection surface (Q_{loss}) indeed determine the evaporator's operating temperature, T_e.

Foam ligaments are all interconnected, and thus heat transferred from hot vapor flow to ligaments in the central region of a vapor passage can directly reach the joints between foam ligaments and envelope by conductive spreading. In contrast, such conductive spreading is limited via sintered copper powders for OEM heat pipes. Further, condensate flow whose temperature is lower than the vapor flow (but much higher than the ambient temperature), also transfers heat to the inner surface of the envelope, which is expected to be much higher than that in OEM heat pipes due to substantial enhancement by foam ligaments protruding internally from the envelope. The foam ligaments hence provide an enlarged heat transfer area ($A_{M\text{-}S}$, m^2) and an increased convective heat transfer

Downloaded from http://asmedigitalcollection.asme.org/heattransfer/article-pdf/doi/10.1115/1.4065352/7332717/ht_146_08_081602.pdf by The Nanjing University Of Aeronautics & Astronautics user on 07 May 2024

coefficient ($h_{M\text{-}S}$, W/m^{2}K) over the sinter powder wick structure. As a result, the heat loss (Q_{loss}) through the ultrathin-walled envelope of the midsection becomes substantial compared to the OEM heat pipe. Consequently, both the increased Q_{loss} and the reduced thermal resistance (R_θ(uFHP) = (1/3)R_θ(OEM)) in Eq. (12) act to lower the evaporator's operating temperature, T_e as observed in Fig. 7(*c*).

4 Conclusions

Based upon a new design strategy for capillary-driven heat pipes that are tailorable, lightweight, and thermally effective, we advanced a thermal solution with such a heat pipe constituted by an ultrathin-walled envelope and foam core for vapor passaging and condensate wicking – an ultrathin-walled foam heat pipe (uFHP). We documented the detailed fabrication and characterization procedures. The high porosity foam core tailored for a noncircular cross section and ultrathin envelope by blackening make a lightweight capillary-driven heat pipe, approximately 64% lighter than commercial heat pipes wicked by sintered Cu powders, with similar dimensions. Due to additional heat rejection through the ultrathin-walled envelope of ~50 μm, the evaporator of the uFHP operates at 15% lower temperature with 70% lower thermal resistance than commercial heat pipes in the input heat range from 5.0 W to 40.0 W. The uFHP can be tailored into any cross-sectional (e.g., noncircular) shape, albeit with a thin-walled envelope, due to the pore-base mechanical support from foam ligaments. This tailorable uFHP can provide an alternative, flexible heat pipe thermal solution for extremly compact operations.

Funding Data

- Ministry of Science and ICT of Korea via the National Research Foundation of Korea (Grant No. 2021R1A2C3007705).

Data Availability Statement

The datasets generated and supporting the findings of this article are obtainable from the corresponding author upon reasonable request.

Nomenclature

$A_{M\text{-}S}$ = enhanced heat transfer area, m^2
d_{cell} = cell size of Cu foam, mm
d_{pore} = pore size of Cu foam, mm
FR = ratio of the volume of DI water used in the heat pipe to the empty volume
g = gravitational acceleration, m/s^2
h = height of capillary rise, mm
H_e = height of heat pipe, mm
$h_{M\text{-}S}$ = increased convective heat transfer coefficient, W/m^{2}K
K = permeability of metal foams, μm^2
L = length of heat pipe, mm
l_a = length of foam ligaments, mm
l_t = thickness of foam ligaments, mm
m = total weight of heat pipe, g
Q_{in} = input heat, W
Q_{loss} = heat loss through the mid-section surface of heat pipe, W
Q_{out} = removed heat, W
R = electrical resistance of heater, Ω
r_{eff} = effective capillary radius of metal foams, μm
R_θ = thermal resistance, K/W
s = distance from evaporator end along the span of heat pipe, mm
T = surface temperature of heat pipe from film thermocouple, ° C
t = time of capillary rise, s
T_∞ = ambient temperature, ° C
T_c = average temperatures of the condenser, ° C
T_e = average temperatures of the evaporator, ° C
T_{IR} = temperature value from IR camera, ° C
U = overall heat transfer coefficient W/m^2 K
V = voltage supplied to the heater, V
V_e = external volume of heat pipe, cm^3
W_e = width of heat pipe, mm
ΔP_c = capillary pressure, N/m^2

Greek Symbols

α = the angle between heat pipe axis (*s*-axis) and gravitational axis (g-axis), deg
δ = wall thickness of envelop, μm
ε = porosity of metal foams
θ = contact angle, deg
σ = surface tension of DI water, N/m
μ = viscosity of DI water, Pa·s
ρ = density of DI water, g/cm^3
ρ_{eff} = effective density, g/cm^3

Subscripts

uFHP = ultralight foam heat pipe
OEM = original equipment manufacturer heat pipe

Appendix A: Topological Parameter

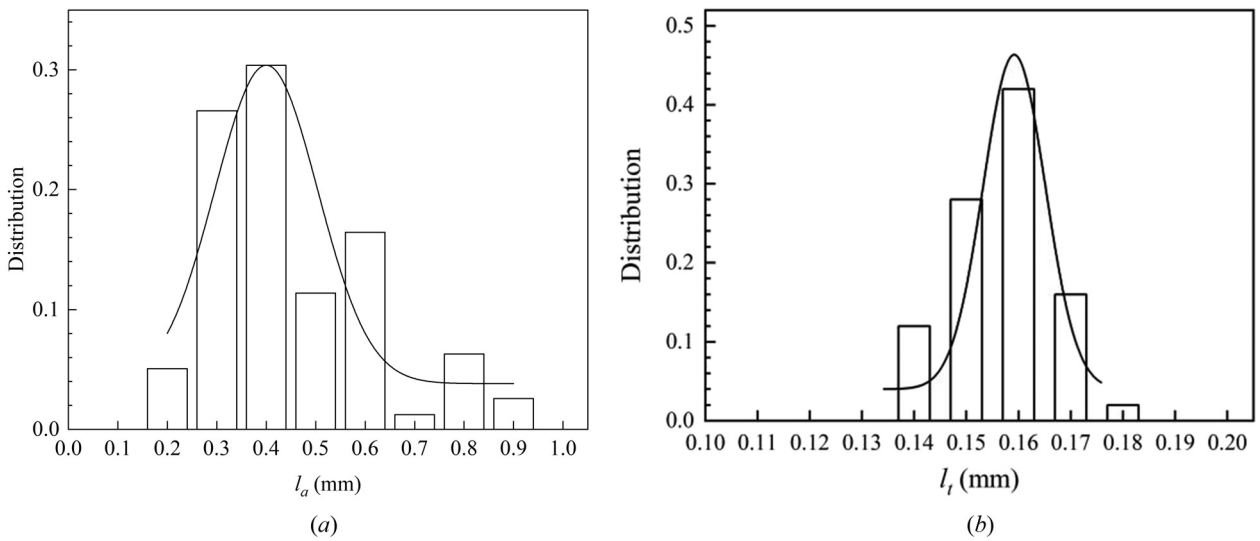


Fig. 8 Open-cell copper (Cu) foam with 60 pores per inch (PPI): (*a*) Distribution of ligament length (l_a) (mean: 0.412 mm ±0.009 and (*b*) distribution of ligament thickness (l_t) (mean: 0.159 mm ±0.002)

Downloaded from http://asmedigitalcollection.asme.org/heattransfer/article-pdf/doi/10.1115/1.4065352/7332717/ht_146_08_081602.pdf by The Nanjing University Of Aeronautics & Astronautics user on 07 May 2024

Appendix B: Optimal Filling Ratio (FR)

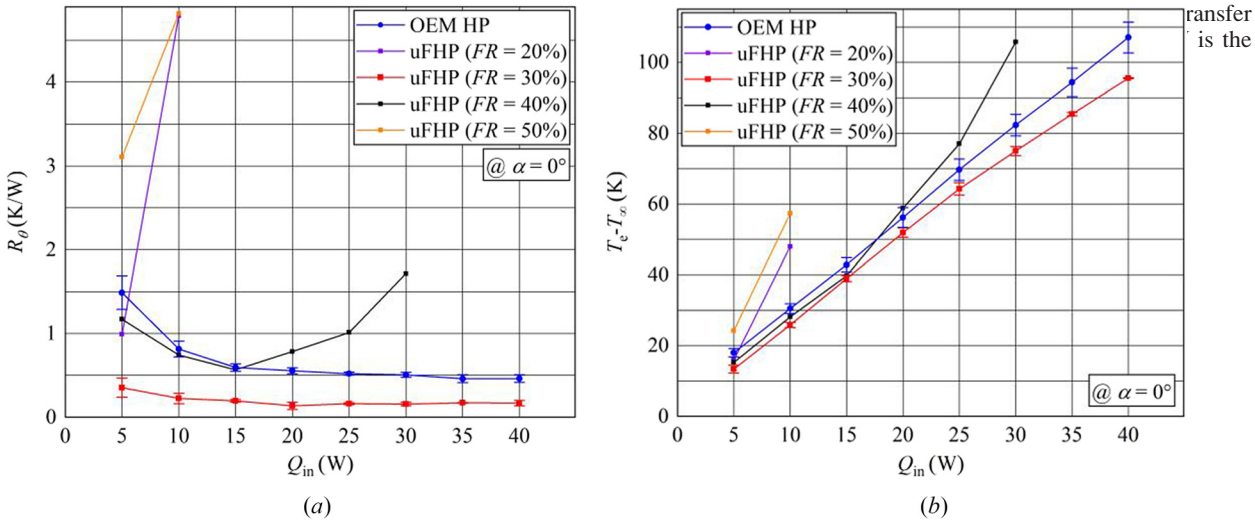


Fig. 9 Effect of filling ratios (FR) at $\alpha = 0$ deg: (*a*) thermal resistance (R_θ) and (*b*) mean evaporator temperature (T_e–T_∞)

Appendix C: Heat Rejection Through an Ultrathin-Walled Envelope

We consider a generic capillary-driven heat pipe with heating power (Q_{in}) input imposed on the evaporator end running at an average temperature (T_e) as illustrated in Fig. 10. In the midsection, there is heat loss (Q_{loss}) through the envelope wall to the surroundings at ambient conditions: heat transfer occurs through the heat pipe wall to the surroundings. The condenser end has an average temperature (T_c) where heat is removed (Q_{out}) via convective cooling. The objective is to demonstrate with energy balance considerations how the operating temperature of the evaporator (T_e) is related to the heat loss (Q_{loss}) through the M-S wall. It should be noted that in the conventional thermodynamic analysis for capillary-driven heat pipes, the heat loss is typically assumed to be negligible as being adiabatic, i.e., ($Q_{loss} = 0$).

Using the conservation of energy, the input power (Q_{in}) is equal to the sum of heat loss (Q_{loss}) and heat rejected (Q_{out}) from the condenser end as

$$Q_{in} = Q_{out} + Q_{loss} \tag{C1}$$

The input heating power (Q_{in}) is also related to the overall thermal resistance (R_θ) across the evaporator and the condenser by definition as

$$R_\theta = \frac{T_e - T_c}{Q_{in}} \Rightarrow Q_{in} = \frac{T_e - T_c}{R_\theta} \tag{C2}$$

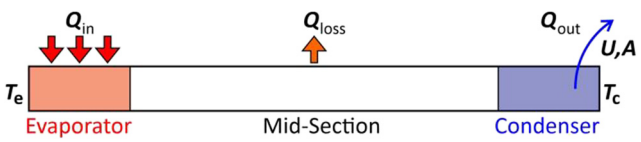


Fig. 10 Schematic of a heat pipe that shows the evaporator operating temperature and the respective heat flows *into* and *out* of the heat pipe

overall heat transfer coefficient and A is the heat transfer area as expressed

$$Q_{out} = UA(T_c - T_\infty) \tag{C3}$$

Substitution of Eqs. (C2 and C3) into Eq. (C1) yields

$$\frac{T_e - T_c}{R_\theta} = UA(T_c - T_\infty) + Q_{loss} \tag{C4}$$

Further simplifying and re-arranging Eq. (C3) for the evaporator temperature (T_e) lead to

$$T_e = (1 + R_\theta UA)T_c - R_\theta UAT_\infty + R_\theta Q_{loss} \tag{C5}$$

From Eq. (C2), the condenser temperature (T_c) is found to be

$$R_\theta = \frac{T_e - T_c}{Q_{in}} \Rightarrow T_c = T_e - R_\theta Q_{in} \tag{C6}$$

Substitution of Eq. (C6) into Eq. (C5) gives

$$T_e = (1 + R_\theta UA)(T_e - R_\theta Q_{in}) - R_\theta UAT_\infty + R_\theta Q_{loss} \tag{C7}$$

Equation (C7) can be reduced to

$$T_e = \frac{Q_{in}}{UA} + R_\theta Q_{in} + T_\infty - \frac{Q_{loss}}{UA} \tag{C8}$$

The final expression, Eq. (C8) explicitly indicates that for given heat input through the evaporator end (Q_{in}) and heat rejection at the condenser end by convection ($UA(T_c - T_\infty)$) of a heat pipe, both thermal resistance along the heat pipe span (R_θ) and heat loss through the midsection surface (Q_{loss}) indeed determine the evaporator's operating temperature, T_e.

References

[1] Faghri, A., 2012, "Review and Advances in Heat Pipe Science and Technology," ASME J. Heat Transfer, **134**(12), p. 123001.

Downloaded from http://asmedigitalcollection.asme.org/heattransfer/article-pdf/doi/10.1115/1.4065352/7332717/ht_146_08_081602.pdf by The Nanjing University Of Aeronautics & Astronautics user on 07 May 2024

[2] Faghri, A., 2014, "Heat Pipes: Review, Opportunities and Challenges," Front. Heat Pipes, **5**(1), pp. 1–48.
[3] Celsia, 2023, "Types of Heat Pipes," Celsia Inc., Harbeson, DE, accessed Apr. 24, 2024, https://celsiainc.com/heat-sink-blog/types-of-heat-pipes
[4] Leong, K. C., Liu, C. Y., and Lu, G. Q., 1997, "Characterization of Sintered Copper Wicks Used in Heat Pipes," J. Porous Mater., **4**(4), pp. 303–308.
[5] Kamotani, Y., 1976, "Analysis of Axially Grooved Heat Pipe Condensers," 14th Aerospace Sciences Meeting, Washington, DC, Jan. 26–28.
[6] Morooka, S., Kuroki, T., and Waki, T., 1981, "Study on the Heat Pipe. III—Heat Transfer Mechanism in the Evaporator of Heat Pipe With Screen Mesh Wick," Bull. JSME, **24**(196), pp. 1811–1819.
[7] Semenic, T., and Catton, I., 2009, "Experimental Study of Biporous Wicks for High Heat Flux Applications," Int. J. Heat Mass Transfer, **52**(21–22), pp. 5113–5121.
[8] Chan, C. W., Siqueiros, E., Ling-Chin, J., Royapoor, M., and Roskilly, A. P., 2015, "Heat Utilisation Technologies: A Critical Review of Heat Pipes," Renew Sust. Energ. Rev., **50**, pp. 615–627.
[9] Tang, H., Lian, L., Zhang, J., and Liu, Y., 2019, "Heat Transfer Performance of Cylindrical Heat Pipes With Axially Graded Wick at Anti-Gravity Orientations," Appl. Therm. Eng., **163**, p. 114413.
[10] Li, Y., Chen, S., He, B., Yan, Y., and Li, B., 2016, "Effects of Vacuuming Process Parameters on the Thermal Performance of Composite Heat Pipes," Appl. Therm. Eng., **99**, pp. 32–41.
[11] Chen, B. B., Liu, W., Liu, Z. C., Li, H., and Yang, J. G., 2012, "Experimental Investigation of Loop Heat Pipe With Flat Evaporator Using Biporous Wick," Appl. Therm. Eng., **42**, pp. 34–40.
[12] Wu, S. C., Wang, D., Lin, W. J., and Chen, Y. M., 2015, "Investigating the Effect of Powder-Mixing Parameter in Biporous Wick Manufacturing on Enhancement of Loop Heat Pipe Performance," Int. J. Heat Mass Transfer, **89**, pp. 460–467.
[13] Han, X. H., Wang, Q., Park, Y. G., T'Joen, C., Sommers, A., and Jacobi, A., 2012, "A Review of Metal Foam and Metal Matrix Composites for Heat Exchangers and Heat Sinks," Heat Transfer Eng., **33**(12), pp. 991–1009.
[14] Zhou, W., Ling, W., Duan, L., Hui, K. S., and Hui, K. N., 2016, "Development and Tests of Loop Heat Pipe With Multi-Layer Metal Foams as Wick Structure," Appl. Therm. Eng., **94**, pp. 324–330.
[15] Tang, Y., Tang, H., Li, J., Zhang, S., Zhuang, B., and Sun, Y., 2017, "Experimental Investigation of Capillary Force in a Novel Sintered Copper Mesh Wick for Ultra-Thin Heat Pipes," Appl. Therm. Eng., **115**, pp. 1020–1030.
[16] Jiang, L. L., Tang, Y., Zhou, W., Jiang, L. Z., Xiao, T., Yan, L., and Gao, J. W., 2014, "Design and Fabrication of Sintered Wick for Miniature Cylindrical Heat Pipe," Trans. Nonferrous Met. Soc. China, **24**(1), pp. 292–301.
[17] Tang, H., Tang, Y., Wan, Z., Li, J., Yuan, W., Lu, L., Li, Y., and Tang, K., 2018, "Review of Applications and Developments of Ultra-Thin Micro Heat Pipes for Electronic Cooling," Appl. Energy, **223**, pp. 383–400.
[18] Cui, Z., Jia, L., Wang, Z., Dang, C., and Yin, L., 2022, "Thermal Performance of an Ultra-Thin Flat Heat Pipe With Striped Super-Hydrophilic Wick Structure," Appl. Therm. Eng., **208**, p. 118249.
[19] Li, J., and Lv, L., 2016, "Experimental Studies on a Novel Thin Flat Heat Pipe Heat Spreader," Appl. Therm. Eng., **93**, pp. 139–146.
[20] Phillips, E. C., "Low-Temperature Heat Pipe Research Program," NTRS, Santa Monica, CA, Paper No. NAS1-8000.
[21] Carbajal, G., Sobhan, C. B., Peterson, G. P., Queheillalt, D. T., and Wadley, H. N. G., 2006, "Thermal Response of a Flat Heat Pipe Sandwich Structure to a Localized Heat Flux," Int. J. Heat Mass Transfer, **49**(21–22), pp. 4070–4081.
[22] Queheillalt, D. T., Carbajal, G., Peterson, G. P., and Wadley, H. N. G., 2008, "A Multifunctional Heat Pipe Sandwich Panel Structure," Int. J. Heat Mass Transfer, **51**(1–2), pp. 312–326.
[23] Hansen, G., and Næss, E., 2015, "Performance of Compressed Nickel Foam Wicks for Flat Vertical Heat Pipes," Appl. Therm. Eng., **81**, pp. 359–367.
[24] Dhanabal, S., Annamalai, M., and Muthusamy, K., 2017, "Experimental Investigation of Thermal Performance of Metal Foam Wicked Flat Heat Pipe," Exp. Therm. Fluid Sci., **82**, pp. 482–492.
[25] Shirazy, M. R. S., and Fréchette, L. G., 2010, "A Parametric Investigation of Operating Limits in Heat Pipes Using Novel Metal Foams as Wicks," Eighth International Conference on Nanochannels, Microchannels, and Minichannels, ASME Paper No. FEDSM-ICNMM2010-31268.
[26] Shirazy, M. R. S., and Fréchette, L. G., 2013, "Capillary and Wetting Properties of Copper Metal Foams in the Presence of Evaporation and Sintered Walls," Int. J. Heat Mass Transfer, **58**(1–2), pp. 282–291.
[27] Tang, H., Xie, Y., Xia, L., Tang, Y., and Sun, Y., 2023, "Review on the Fabrication of Surface Functional Structures for Enhancing Heat Transfer of Heat Pipes," Appl. Therm. Eng., **226**, p. 120337.
[28] Nam, Y., and Ju, Y. S., 2013, "A Comparative Study of the Morphology and Wetting Characteristics of Micro/Nanostructured Cu Surfaces for Phase Change Heat Transfer Applications," J. Adhes. Sci. Technol., **27**(20), pp. 2163–2176.
[29] Shum, C., Rosengarten, G., and Zhu, Y., 2017, "Enhancing Wicking Microflows in Metallic Foams," Microfluid. Nanofluid., **21**(12), p. 177.
[30] Yang, H., Yang, Y., Ma, B., and Zhu, Y., 2022, "Experimental Study on Capillary Microflows in High Porosity Open-Cell Metal Foams," Micromachines, **13**(12), p. 2052.
[31] Yang, X. H., Kuang, J. J., Lu, T. J., Han, F. S., and Kim, T., 2013, "A Simplistic Analytical Unit Cell-Based Model for the Effective Thermal Conductivity of High Porosity Open-Cell Metal Foams," J. Phys. D: Appl. Phys., **46**(25), p. 255302.
[32] Klostermann, J., Schwarze, R., and Brücker, C., 2013, "Meshing of Porous Foam Structures on the Micro-Scale," Eng. Comput., **29**(1), pp. 95–110.
[33] Min, J., Wu, X., Shen, L., and Gao, F., 2011, "Hydrophilic Treatment and Performance of Copper Finned Tube Evaporators," Appl. Therm. Eng., 31 (14–15), pp. 2936–2942.
[34] Zohuri, B., 2011, "Heat Pipe Theory and Modeling," *Heat Pipe Design and Technology*, CRC Press, Boca Raton, FL, pp. 144–151.
[35] Youn, Y. J., and Kim, S. J., 2012, "Fabrication and Evaluation of a Silicon-Based Micro Pulsating Heat Spreader," Sensor Actuat. A: Phys., **174**, pp. 189–197.
[36] Tang, Y., Deng, D., Lu, L., Pan, M., and Wang, Q., 2010, "Experimental Investigation on Capillary Force of Composite Wick Structure by IR Thermal Imaging Camera," Exp. Therm. Fluid Sci., **34**(2), pp. 190–196.
[37] Coleman, H. W., and Steele, W. G., 2018, "Uncertainty in a Result Determined From Multiple Variables," *Experimentation, Validation, and Uncertainty Analysis for Engineers*, Wiley, Hoboken, NJ.
[38] Li, H., Fang, X., Li, G., Zhou, G., and Tang, Y., 2018, "Investigation on Fabrication and Capillary Performance of Multi-Scale Composite Porous Wick Made by Alloying-Dealloying Method," Int. J. Heat Mass Transfer, **127**, pp. 145–153.
[39] Khayargoli, P., Loya, V., Lefebvre, L. P., and Medraj, M., 2004, "The Impact of Microstructure on the Permeability of Metal Foams," CSME 2004 Forum, London, ON, Canada, pp. 220–228.
[40] Bhattacharya, A., Calmidi, V. V., and Mahajan, R. L., 2002, "Thermophysical Properties of High Porosity Metal Foams," Int. J. Heat Mass Transfer, **45**(5), pp. 1017–1031.
[41] Majumdar, A., and Bhushan, B., 1990, "Role of Fractal Geometry in Roughness Characterization and Contact Mechanics of Surfaces," ASME J. Tribol., **112**(2), pp. 205–216.
[42] Plessis, P. D., Montillet, A., Comiti, J., and Legrand, J., 1994, "Pressure Drop Prediction for Flow Through High Porosity Metallic Foams," Chem. Eng. Sci., **49**(21), pp. 3545–3553.
[43] Garrido, G. I., Patcas, F. C., Lang, S., and Kraushaar-Czarnetzki, B., 2008, "Mass Transfer and Pressure Drop in Ceramic Foams: A Description for Different Pore Sizes and Porosities," Chem. Eng. Sci., **63**(21), pp. 5202–5217.
[44] Hwang, J. J., Hwang, G. J., Yeh, R. H., and Chao, C. H., 2002, "Measurement of Interstitial Convective Heat Transfer and Frictional Drag for Flow Across Metal Foams," ASME J. Heat Mass Transfer-Trans. ASME, **124**(1), pp. 120–129.
[45] Mancin, S., Zilio, C., Rossetto, L., and Cavallini, A., 2011, "Foam Height Effects on Heat Transfer Performance of 20 ppi Aluminum Foams," Appl. Therm. Eng., **49**, pp. 55–60.
[46] Zafari, M., Panjepour, M., Meratian, M., and Emami, M. D., 2016, "CFD Simulation of Forced Convective Heat Transfer by Tetrakaidecahedron Model in Metal Foams," J. Porous Media, **19**(1), pp. 1–11.
[47] Wu, Z., Caliot, C., Bai, F., Flamant, G., Wang, Z., Zhang, J., and Tian, C., 2010, "Experimental and Numerical Studies of the Pressure Drop in Ceramic Foams for Volumetric Solar Receiver Applications," Appl. Energy, **87**(2), pp. 504–513.
[48] Fries, N., and Dreyer, M., 2008, "An Analytic Solution of Capillary Rise Restrained by Gravity," J. Colloid Interface Sci., **320**(1), pp. 259–263.
[49] Maziuk, V., Kulakov, A., Rabetsky, M., Vasiliev, L., and Vukovic, M., 2001, "Miniature Heat-Pipe Thermal Performance Prediction Tool – Software Development," Appl. Therm. Eng., **21**(5), pp. 559–571.
[50] Park, K., Lee, W., Lee, K., Baek, I., Rhi, S., and Shin, D., 2005, "Study on the Operating Characteristics in Small Size Heat Pipe Using Nanofluids," Proceedings of the Third IASME/WSEAS International Conference on Heat Transfer, Thermal Engineering and Environment, Corfu, Greece, Aug. 20–25, pp. 106–109.
[51] Wong, S., Hsu, Z., and Hsu, L., 2017, "On the Test Setting at Condenser in Thermal Performance Tests of Heat Pipes," ASME Paper No. FEDSM2017-69517.
[52] Mahdavi, M., Tiari, S., Schampheleire, S. D., and Qiu, S., 2018, "Experimental Study of the Thermal Characteristics of a Heat Pipe," Exp. Therm Fluid Sci., **93**, pp. 292–304.

Downloaded from http://asmedigitalcollection.asme.org/heattransfer/article-pdf/doi/10.1115/1.4065352/7332717/ht_146_08_081602.pdf by The Nanjing University Of Aeronautics & Astronautics user on 07 May 2024